Article

Numerical Analysis of Leading-Edge Roughness Effects on the Aerodynamic Performance of a Thick Wind Turbine Airfoil

Wei Zhang [1], Kuichao Ma [2], Chang Cai [3,4,*], Xiangyu Sun [3,4], Jun Zhang [2], Xiaohui Zhong [3,4,5], Xiaomin Rong [3,4] and Qing'an Li [3,4,5,*]

[1] Institute of Engineering and Technology, Hangzhou Huadian Engineering Consulting Co., Ltd., Hangzhou 310030, China
[2] New Energy Research Center, Huadian Electric Power Research Institute Co., Ltd., Hangzhou 310030, China
[3] Institute of Engineering Thermophysics, Chinese Academy of Sciences, Beijing 100190, China
[4] The Key Laboratory of Wind Energy Utilization of Chinese Academy of Sciences, Beijing 100190, China
[5] School of Engineering Science, University of Chinese Academy of Sciences, Beijing 100049, China
* Correspondence: caichang@iet.cn (C.C.); liqingan@iet.cn (Q.L.)

Abstract: The aerodynamic performance of wind turbine airfoils is crucial for the efficiency and reliability of wind energy systems, with leading-edge roughness significantly impacting blade performance. This study conducts numerical simulations on the DU 00-W-401 airfoil to investigate the effects of leading-edge roughness. Results reveal that the rough airfoil exhibits a distinctive "N"-shaped lift coefficient curve. The formation mechanism of this nonlinear lift curve is primarily attributed to the development of the trailing-edge separation vortex and variations in the adverse pressure gradient from the maximum thickness position to the trailing-edge confluence. The impact of different roughness heights is further investigated. It is discovered that when the roughness height is higher than 0.3 mm, the boundary layer can be considered fully turbulent, and the lift curve shows the "N" shape stably. When the roughness height is between 0.07 mm and 0.1 mm, a transitional state can be observed, with several saltation points in the lift curve. The main characteristics of different flow regimes based on different lift curve segments are summarized. This research enhances the understanding of the effects of leading-edge roughness on the aerodynamic performance of a thick wind turbine airfoil, and the simulation method for considering the effect of leading-edge roughness is practical to be applied on large-scale wind turbine blade to estimate the aerodynamic performance under rough leading-edge conditions, thereby supporting advancements in wind turbine technology and promoting the broader adoption of renewable energy.

Keywords: wind turbine; thick airfoil; leading-edge roughness; aerodynamic performance

1. Introduction

The aerodynamic performance of wind turbine airfoils is crucial for the efficiency and reliability of wind energy systems. As horizontal-axis wind turbines continue to grow in size, structural requirements necessitate the use of thicker airfoils at the mid-span and inner positions of the blades. Currently, the relative thickness of airfoils used in the middle of large wind turbine blades is approximately 25%, increasing further towards the blade root to about 40% [1,2]. In contrast, traditional aviation airfoils typically have a relative thickness of no more than 15% [3]. Early blade designs achieved thicker airfoils by linearly scaling up thinner aviation airfoils, which often resulted in suboptimal aerodynamic performance [4].

To address these challenges, institutions have developed specialized wind turbine airfoil families, such as the NREL S-series [5], DU-series [6], FFA-W-series [7], and Risø-series airfoils [8]. These designs take into account a comprehensive range of factors, including lift-to-drag ratio, maximum lift coefficient, stall characteristics, roughness sensitivity, and geometric and structural compatibility [6,9–11]. Compared to earlier airfoils, these modern designs have demonstrated significantly improved overall performance.

Among various design considerations, the leading edge of an airfoil plays a significant role in determining its aerodynamic characteristics. Leading-edge roughness, in particular, can substantially influence the performance of wind turbine blades. Leading-edge roughness refers to surface irregularities or textures that are intentionally or unintentionally present along the leading edge of an airfoil. These roughness elements can arise from manufacturing imperfections, environmental exposure, or intentional design modifications [12,13]. It is generally believed that leading-edge roughness induces boundary layer transition, increasing its thickness and thus the drag coefficient [14]. It also reduces the effective camber of the airfoil, lowering its aerodynamic performance [15]. When the size of the rough elements is large enough, they can cause early boundary layer separation, leading to premature stall and a substantial decrease in aerodynamic efficiency [16].

For thick wind turbine airfoils, one of the effects of leading-edge roughness is the potential to cause a significantly non-linear lift coefficient curve around a zero degrees angle of attack. This phenomenon has been documented by several researchers through wind tunnel tests of airfoils such as the DU 00-W-350, DU 00-W-401 [17], and FB-3500-0050 [18]. With rough leading edges, the lift curves of these airfoils undergo significant changes. The lift coefficient is higher than that of smooth leading edges in the negative angle of attack region. Near a 0° angle of attack, the lift coefficient exhibits a local negative slope segment and drops abruptly at various points. As the angle of attack continues to increase, the lift coefficient increases slowly. Compared to smooth leading-edge conditions, the overall performance of the airfoil is noticeably reduced. The special nonlinear lift performance can also be observed on thick airfoils at relatively low Reynolds numbers, as reported by Hansen et al. [19].

The above literature review highlights the significant impact of leading-edge roughness on the aerodynamic performance of wind turbine airfoils, with a particular focus on thick airfoils where leading-edge roughness can induce a nonlinear lift curve around 0° AOA. While most existing research has been conducted through wind tunnel aerodynamics tests, there is a notable gap in numerical research. The formation mechanisms and influencing factors of the observed effects have not been fully understood. In response to this gap, the current research employs numerical simulations to investigate the impact of leading-edge roughness on wind turbine airfoils. The flow detail and the formation mechanism behind the nonlinear lift curve observed in rough airfoils are elucidated. The simulation method considering the effect of leading-edge roughness is developed and verified, and is practical to be applied on large-scale wind turbine blades to estimate the aerodynamic performance under rough leading-edge conditions. Additionally, the research examines how variations in roughness height affect the nonlinear lift curve, discovering different types of lift curves for the first time, which is inspiring for similar research on the non-linear lift performance of thick airfoils. The insights gained from this study are expected to provide valuable guidance for the design and optimization of wind turbine blades, enhancing their efficiency and effectiveness in harnessing wind energy.

2. Research Objects and Methods

2.1. Research Objects

The dedicated wind turbine airfoil DU 00-W-401 is selected as the calculation object in this research, as it is a typical thick wind turbine airfoil [17]. For the rough airfoil cases, a continuous region around the leading-edge region is set as the rough surface, as shown in Figure 1. The starting and ending position of the roughness follows the experiment scheme of Van Rooij et al. [17], in which bump tapes of 0.5 mm thickness were set at 2% of chord on the upper surface and at 10% of chord on the lower surface. The chord length *c* is 600 mm, and the calculated Reynolds number is 3.0×10^6, corresponding to a freestream inflow velocity 73 m/s.
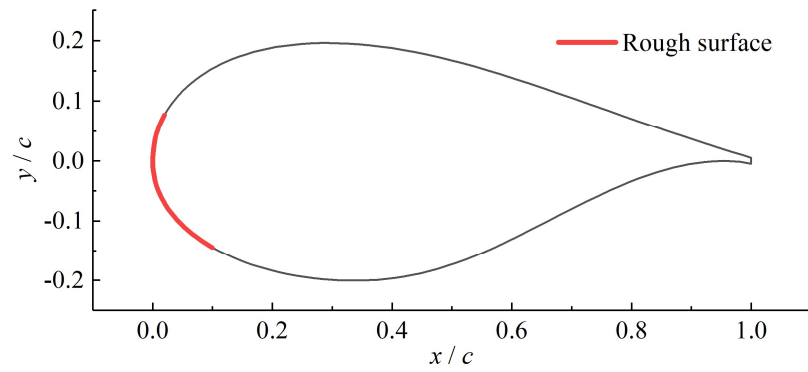
Figure 1. Profile of DU 00-W-401 airfoil and the position of leading-edge roughness.

2.2. Numerical Methods

The numerical simulation was conducted using ANSYS Fluent 2021 R1. A transient, incompressible solver was employed, with turbulence modeled by the four-equation transition shear stress transport (SST) model, which has demonstrated strong performance in related numerical studies [20,21]. The underlying principles and detailed functions of this turbulence model are provided in Refs. [22,23]. For pressure–velocity coupling, the Coupled algorithm was utilized. The spatial discretization of pressure was handled using a Second-Order scheme, while the Third-Order MUSCL scheme was applied for the spatial discretization of both the momentum equations and the turbulence model.

The computational domain is illustrated in Figure 2a. The upper and lower surfaces are $20c$ away from the airfoil and set as the symmetry boundary. The velocity inlet boundary was $20c$ upstream of the airfoil and the pressure outlet boundary was $30c$ downstream of the airfoil. The turbulence intensity at both the inlet and outlet boundaries was set to 0.02% to create a laminar inflow condition, ensuring natural transition for the case with a smooth leading edge. Quadrilateral structured grids were built through an O-type topological structure around the airfoil, as show in Figure 2b. The mesh in the boundary layer was well resolved, with the first layer around the airfoil being 0.01 mm, with a wall normal grid expansion ratio of 1.1. Correspondingly, the value of $y+$ was below 1.0 on the airfoil's surface, which complies with the requirements for applying the current turbulence model [22].
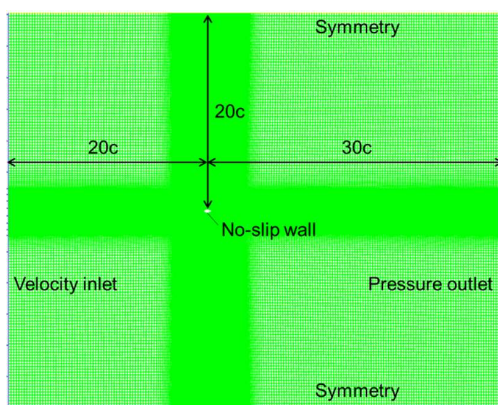
(**a**) Computational domain and boundary condition
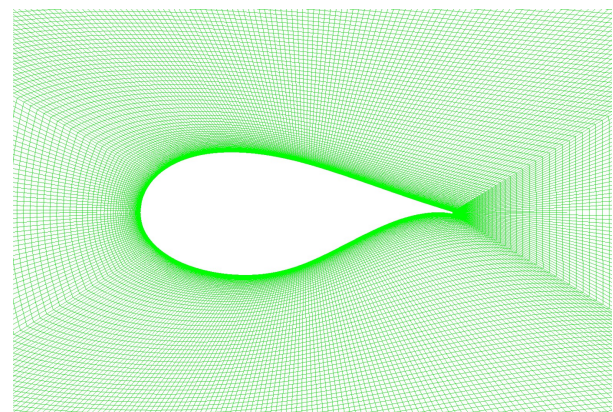
(**b**) Meshing around the airfoil

Figure 2. Mesh and boundary condition.

A time step of 0.001 s was selected, and stable convergence of the lift and drag coefficients was observed across the range of angles of attack considered. Figure 3 illustrates the convergence history of these coefficients at an AOA of 14°. Despite the use of an unsteady scheme, the simulation results demonstrated converged and stable aerodynamic performance without significant unsteady fluctuations. This stable convergence is consistent

with findings from previous work [20,21], which suggests that the turbulence model may have averaged out the unsteady fluctuations, resulting in a stable vortex structure that ultimately converges.
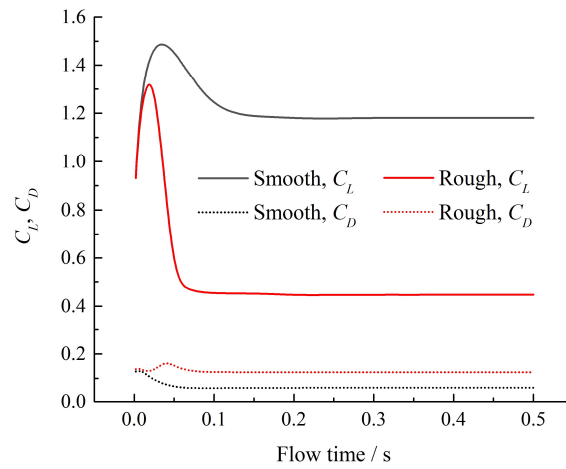
Figure 3. Convergence history of the lift and drag coefficient at 14° AOA.

The mesh independence test confirms that the chosen mesh is adequately refined for accurate results, which is shown in Table 1. As shown in Figure 2, the mesh around the airfoil in the mainstream region is refined. According to the general mesh size in the refined region, three mesh configurations—Dense (5 mm), Medium (10 mm), and Coarse (40 mm)—were evaluated. The Dense mesh showed less than a 1% difference in lift and drag coefficients compared to the Medium mesh, indicating minimal accuracy gains from further refinement. In contrast, the Coarse mesh exhibited around a 4% difference, highlighting a significant drop in accuracy. Additionally, varying the wall normal grid expansion ratio revealed that a lower ratio (1.05) maintained accuracy, while a higher ratio (1.2) led to notable discrepancies. Thus, the Medium mesh with the wall normal grid expansion ratio 1.1 shows its balanced resolution in both the mainstream and boundary layer regions, which was deemed optimal for this study, offering an effective compromise between computational efficiency and precision.

Table 1. Mesh independence verification.

Mesh Density		Medium	Dense	Coarse	Medium	Medium
Wall normal grid expansion ratio		1.1	1.1	1.1	1.05	1.2
AOA = 14°, smooth	C_L	1.1818	1.1800	1.1647	1.1772	1.1145
	C_D	0.06172	0.06184	0.06360	0.06141	0.06685
AOA = 14°, rough	C_L	0.44584	0.44111	0.45604	0.44812	0.44253
	C_D	0.12518	0.12558	0.12807	0.12406	0.12710

2.3. Modelling of the Roughness

Prandtl's roughness model introduces the concept of equivalent sand-grain roughness height K_S [24]. The effect of roughness is incorporated into the log-law of the wall for turbulent boundary layers:

$$\frac{u_p u^*}{\tau_w/\rho} = \frac{1}{\kappa} ln\left(E \frac{\rho u^* y_p}{\mu} \right) - \Delta B$$

where $u^* = C_\mu^{1/4} k^{1/2}$, and ΔB has been found to be well-correlated with the nondimensional roughness height

$$K_S^+ = \rho K_S u^* / \mu$$

where K_S is the physical roughness height and set as 0.5 mm following the height of the bump tape in the experiment of Van Rooij et al. [17].

In Ansys Fluent, the whole roughness regime is subdivided into the three regimes, and the formulas proposed by Cebeci and Bradshaw based on Nikuradse's data are adopted to compute ΔB for each regime [24]. For the aerodynamically smooth regime ($K_S^+ \leq 2.25$),

$$\Delta B = 0$$

For the transitional regime ($2.25 \leq K_S^+ \leq 90$),

$$\Delta B = \frac{1}{\kappa} \ln \left(\frac{K_S^+ - 2.25}{87.75} + C_S K_S^+ \right) \sin \left[0.4258 \left(\ln K_S^+ - 0.811 \right) \right]$$

For the fully rough regime ($K_S^+ > 90$),

$$\Delta B = \frac{1}{\kappa} \ln \left(1 + C_S K_S^+ \right)$$

Except for the wall function modifications, the intermittency transport equation and the turbulence production terms are also adjusted when the roughness effects are incorporated into the transition SST model. For details, refer to Ref. [25].

3. Results and Discussions

3.1. Aerodynamic Performance

The calculated lift coefficients of both smooth and rough airfoils are compared to experimental results by Van Rooij et al. [17], as illustrated in Figure 4. The comparison shows that the numerical results closely match the experimental data, thereby confirming the reliability of the numerical methods used in this research. For the smooth airfoil, the lift coefficient increases linearly around an AOA of 0°. When the AOA exceeds 8°, the lift coefficient curve begins to deviate from this linear trend, indicating the onset of trailing edge separation on the upper surface of the airfoil. In contrast, the rough airfoil's lift coefficient curve exhibits a distinctive "N" shape. Initially, the lift coefficient rises from 0 to 0.6 as the AOA increases from −10° to 0°. Between AOAs of 0° and 5°, a segment with a negative slope in the lift curve is observed. Beyond an AOA of 5°, the lift coefficient continues to rise but at a relatively low rate. The flow pattern and underlying mechanisms responsible for this unique "N" shape in the lift performance of the rough airfoil will be explored in the subsequent subsections.

Some discrepancies between the numerical and experimental results, particularly in the near-stall region, can be observed in Figure 4. These differences may be attributed to the turbulence model used in this study (the four-equation transition SST model), which assumes turbulence is isotropic and may not perform well under conditions of massive flow separation. To achieve greater accuracy in the near-stall and post-stall regions, more advanced numerical methods, such as Large Eddy Simulation (LES), Detached Eddy Simulation (DES), or Scale-Adaptive Simulation (SAS), may yield better results. However, this research primarily focuses on the effects of leading-edge roughness, particularly on the nonlinear lift performance around a 0° angle of attack (AOA). The influence of leading-edge roughness is relatively minor in the post-stall region, where large-scale leading-edge separation vortices dominate. Additionally, one of the objectives of this study is to develop a practical numerical method that can be applied to large-scale wind turbine blades to estimate the impact of leading-edge roughness. For modern large-scale wind turbines equipped with pitch control systems, the blade sections typically operate at relatively low angles of attack. Given these considerations, the current numerical method is deemed sufficient for capturing the primary characteristics induced by leading-edge roughness.
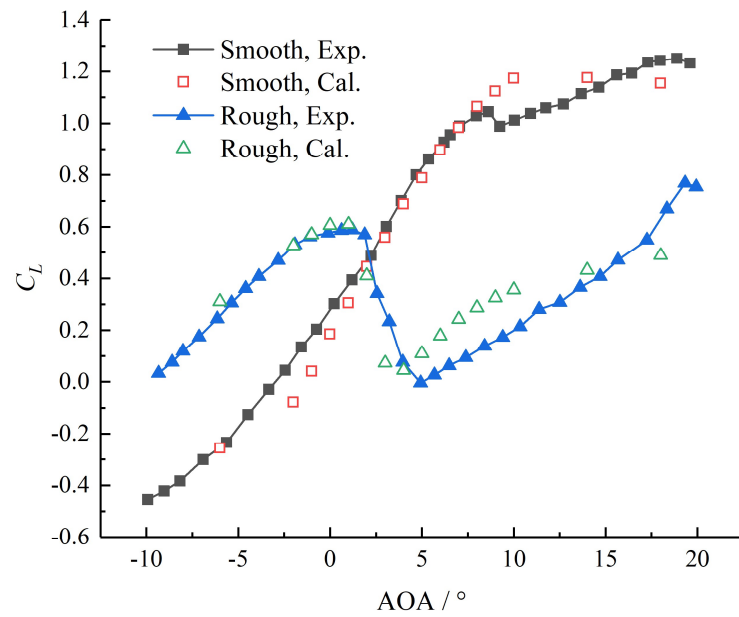
Figure 4. Lift coefficient of the smooth and rough airfoils (experimental data is adapted from Ref. [17]).

Figure 5 displays the calculated drag coefficients for both smooth and rough airfoils. The smooth airfoil exhibits its lowest drag coefficient, approximately 0.01, at an AOA of 0°. The drag coefficient increases as the AOA deviates from 0°, either increasing or decreasing. For AOAs greater than 8°, the drag coefficient rises sharply, attributed to the onset of trailing edge separation on the upper surface and the consequent increase in pressure drag. In contrast, the rough airfoil consistently exhibits a higher drag coefficient curve compared to the smooth airfoil. At AOAs near 0°, where friction drag predominates, the difference in drag coefficient is approximately 0.03, likely due to the increased friction drag caused by the leading-edge roughness. As the AOAs increase, the difference in drag coefficient grows, which may be attributed to changes in the separation condition induced by the roughness at the leading edge, leading to a more significant pressure drag. Notably, there is a slight decrease in the drag coefficient between AOAs of 2° and 4°. The reasons behind this decrease will be examined in the following subsections.
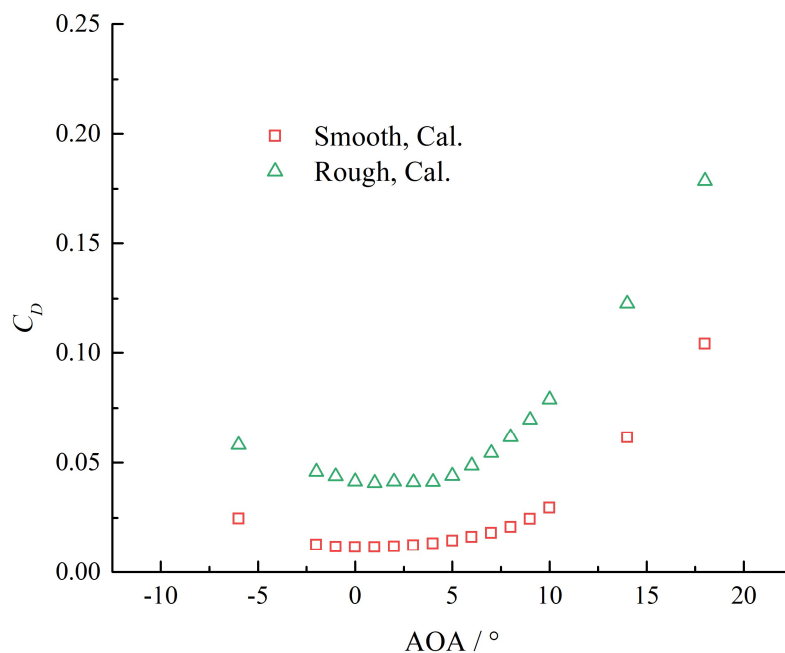
Figure 5. Drag coefficient of the smooth and rough airfoils.

3.2. Flow Patterns

Figure 6 illustrates the contour of turbulence intensity around the smooth airfoil at an AOA of 0°. The boundary layer flow is laminar before reaching halfway along the chord, exhibiting relatively low turbulence intensity. As the flow passes around the mid-chord, the thickness of the region with high turbulence intensity gradually increases, indicating a transition to a turbulent boundary layer. Figure 7 presents the nondimensional streamwise wall shear at this condition, defined by

$$C_{f_x} = \frac{f_x}{0.5\rho U_\infty^2}$$

where f_x is the streamwise wall shear. The value of C_{f_x} is positive if the flow is attached and negative for reversed flow, providing an intuitive depiction of the laminar separation bubble and turbulent separation point positions. According to Figure 7, the laminar separation bubble is located around 46% of the chord on the lower surface and around 38% of the chord on the upper surface. Beyond these points, the flows reattach and the boundary layer becomes turbulent. This indicates that the turbulence model used in this research can simulate the free-transition condition of airfoils effectively. Additionally, a small trailing-edge separation vortex is observed at around 75% of the chord on the lower surface, while turbulent separation is absent on the upper surface. This phenomenon is due to the higher adverse pressure gradient from the maximum thickness position to the trailing edge on the lower surface.
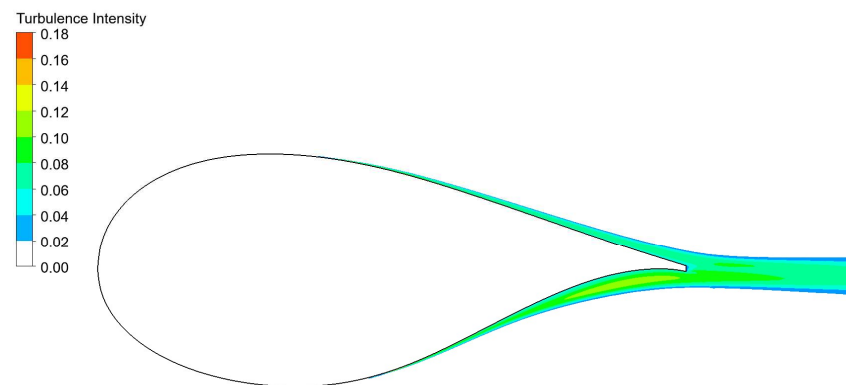
Figure 6. Contour of the turbulence intensity around the smooth airfoil at 0° AOA.
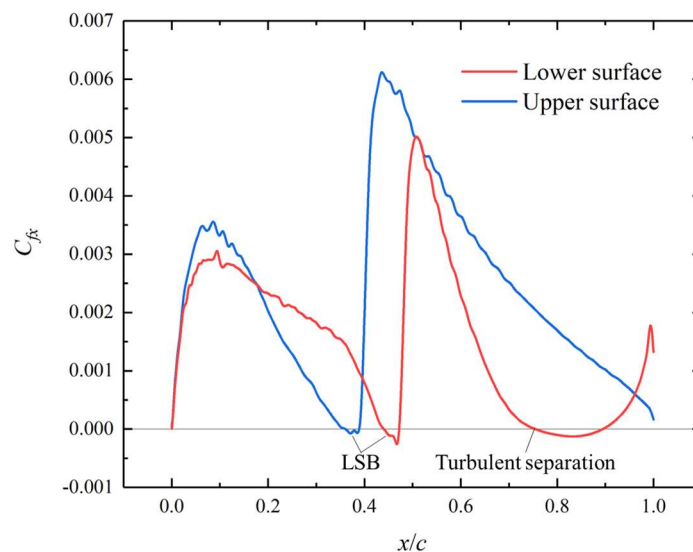
Figure 7. Nondimensional streamwise wall shear around the smooth airfoil at 0° AOA.

Figures 8 and 9 display the contours of turbulence intensity and the nondimensional streamwise wall shear of the rough airfoil at 0° AOA, respectively. Due to the influence of leading-edge roughness, the boundary layer on the rough airfoil is fully turbulent, with regions of high turbulence intensity covering the entire airfoil surface, as seen in Figure 8. This complete transition eliminates the presence of a laminar separation bubble, as observed in Figure 9. This indicates that the primary effect of the leading-edge roughness is to establish a fixed-transition condition, resulting in a turbulent boundary layer over most of the airfoil surface. Figure 9 also reveals that the wall shear around the leading edge of the rough airfoil is significantly higher than that of the smooth airfoil, contributing to the higher drag coefficient seen in Figure 5. When the flow passes the end of the leading-edge roughness, at approximately 2% of the chord (c) on the upper surface and 10% of the chord on the lower surface, there is an abrupt drop in wall shear. The turbulent separation point on the lower surface moves upstream to around 52% of the chord, compared to the smooth airfoil. Additionally, the scale of the trailing-edge separation vortex increases, accompanied by high turbulence intensity. The flow on the upper surface remains attached, similar to the smooth airfoil.
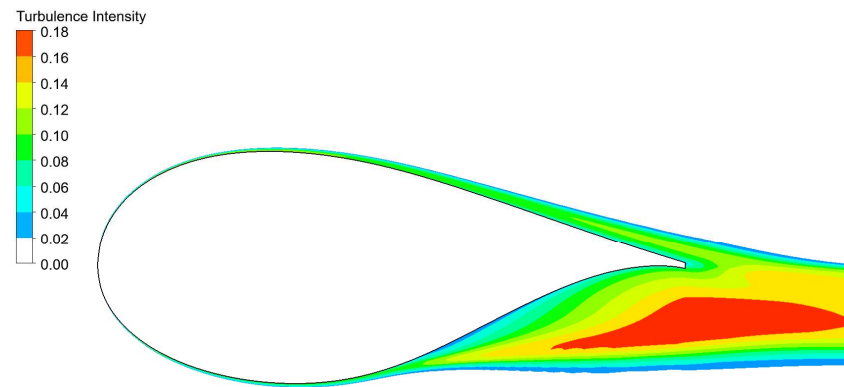
Figure 8. Contour of the turbulence intensity around the rough airfoil at 0° AOA.
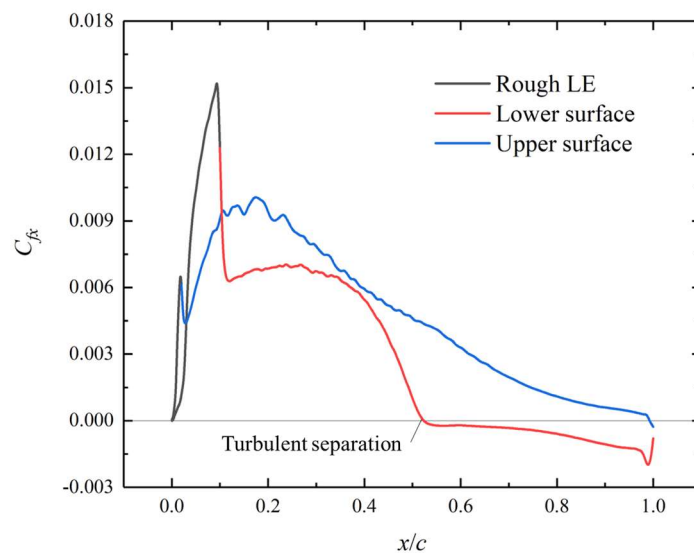
Figure 9. Nondimensional streamwise wall shear around the rough airfoil at 0° AOA.

The streamlines around the smooth and rough airfoils at different AOAs are shown in Figures 10 and 11, respectively. For the smooth airfoil, the flow remains fully attached at AOAs of 0° and 4°, where the lift coefficient curve increases linearly. A trailing-edge separation vortex appears on the lower surface at an AOA of −6°, and on the upper surface at an AOA of 14°, where the lift coefficient curve deviates from its linear increase.

These flow patterns are similar to those observed on traditional thin airfoils of combined trailing-edge and leading-edge stall types.

(**a**) −6°

(**b**) 0°

(**c**) 4°

(**d**) 14°
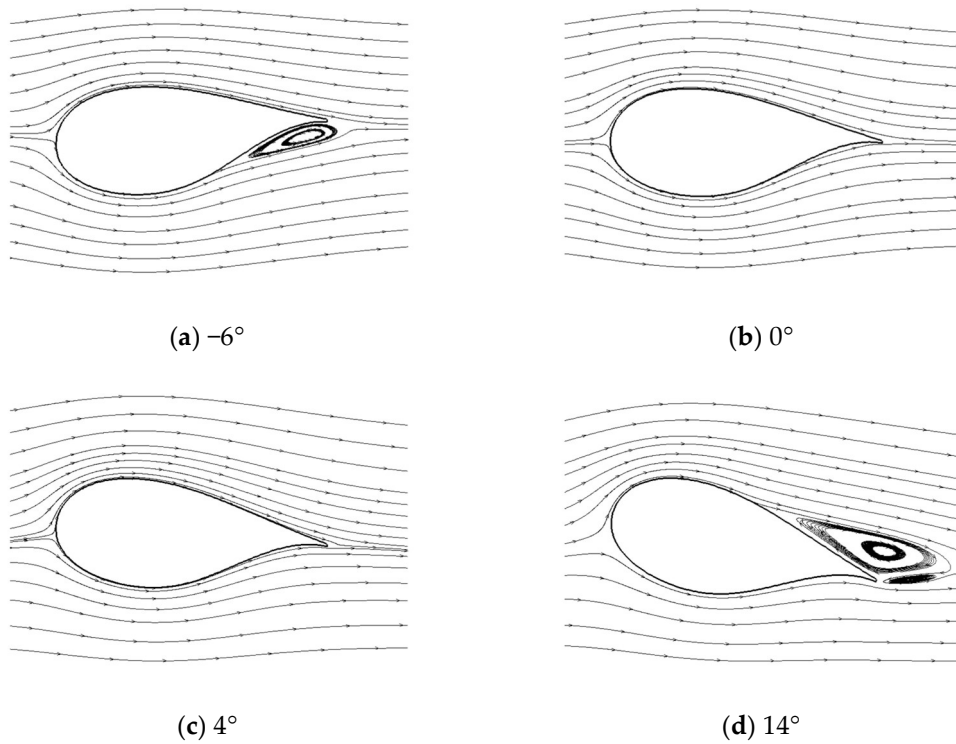
Figure 10. Streamlines around the smooth airfoil at different AOAs.

(**a**) −6°

(**b**) 0°

(**c**) 4°

(**d**) 14°
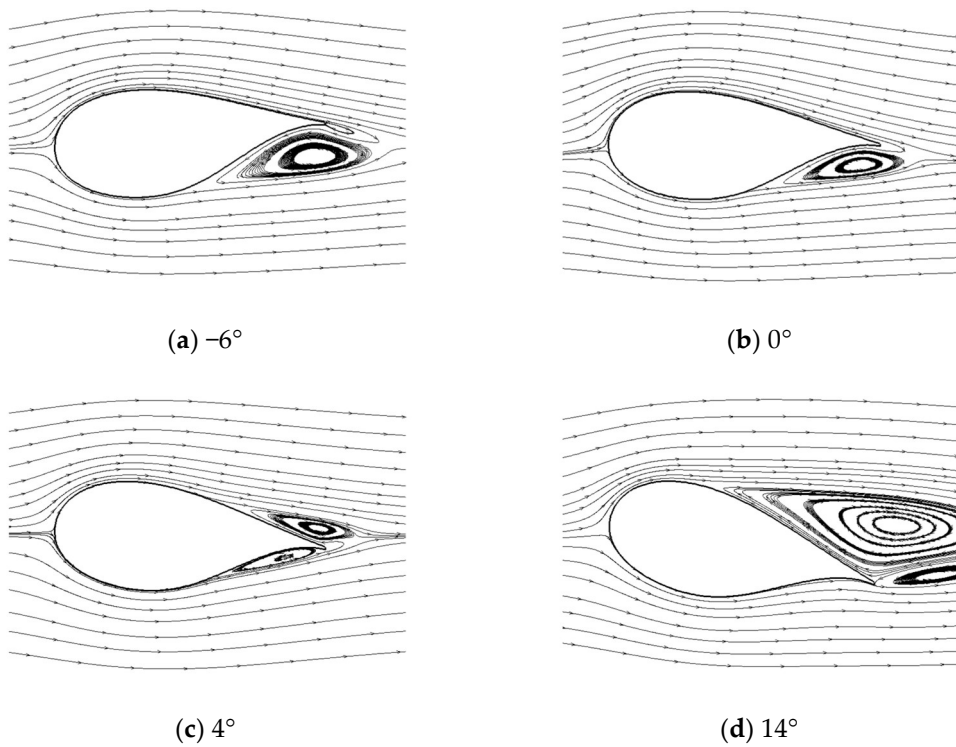
Figure 11. Streamlines around the rough airfoil at different AOAs.

For the rough airfoil, a separation vortex is evident on the lower surface at an AOA of −6°, with the separation point located around the maximum thickness position. The

separation vortex is significantly larger compared to the smooth airfoil. As the AOA increases to $0°$, the separation point on the lower surface remains near the maximum thickness position, while the scale of the separation vortex reduces. With a further increase in AOA to $4°$, the separation point on the lower surface moves downstream to about 2/3 of the chord, and the size of the separation vortex further decreases. Additionally, trailing-edge separation begins to develop on the upper surface, matching the scale of the separation vortex on the lower surface. At an AOA of $14°$, the flow is fully attached to the lower surface, while the separation vortex on the upper surface grows significantly, extending to the entire scale of the airfoil and creating a secondary vortex downstream of the trailing edge. Overall, the flow separation patterns of the rough airfoil differ substantially from those of the smooth airfoil, particularly at AOAs of $0°$ and $4°$ within the negative-slope lift region. The formation mechanism of the negative-slope lift will be further explored in the following subsection.

3.3. Mechanism Discussion on the Nonlinear Lift Performance

To elucidate the formation mechanism of the negative-slope lift performance of the rough airfoil around $0°$ AOA, the pressure contours and streamlines at $0°$ and $4°$ AOA are compared, as shown in Figure 12. The characteristic streamlines between the main stream and the separation vortex were extracted and marked in the figure. Given that the normal pressure variation is minimal in the separation region, the airfoil profile combining these characteristic streamlines can be considered as an enclosed control body, which approximately conforms to potential flow theory. For the lower surface, as the AOA increases from $0°$ to $4°$, the characteristic streamline rises while the trailing-edge separation vortex diminishes. Consequently, the adverse pressure gradient from the maximum thickness position to the trailing-edge confluence increases, resulting in a stronger negative pressure around the maximum thickness on the lower surface. In contrast, on the upper surface, the characteristic streamline also rises but the trailing-edge separation vortex enlarges. This causes a reduction in the adverse pressure gradient from the maximum thickness position to the trailing-edge confluence, leading to a weaker negative pressure around the maximum thickness position. The resulting pressure coefficient distribution is shown in Figure 13. The combined effect of the enhanced negative pressure peak on the lower surface and the weakened negative pressure peak on the upper surface causes a significant drop in airfoil lift as the AOA increases from $0°$ to $4°$, thereby demonstrating a distinct negative-slope lift performance.

(**a**) AOA = $0°$ (**b**) AOA = $4°$
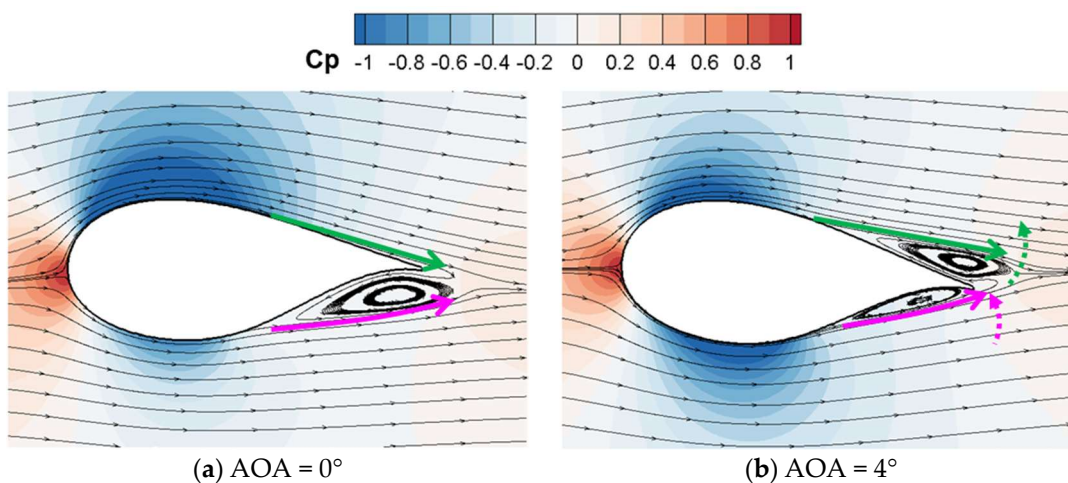
Figure 12. Pressure contour and streamlines around the rough airfoil in the negative-slope lift region. The green and purple arrows represent the characteristic streamlines between the main stream and the separation vortex.
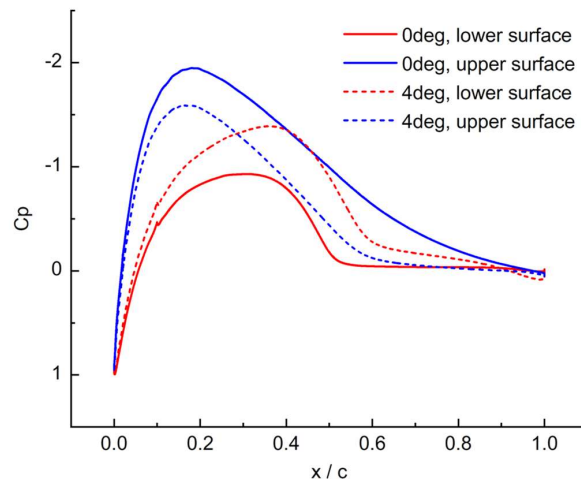
Figure 13. Pressure coefficient distribution on the rough airfoil in the negative-slope lift region.

3.4. Effect of Roughness Height

The aerodynamic performance of smooth and rough airfoils differs significantly, as detailed in the previous subsections. This raises the question of whether a critical state exists between these two performance regimes. To explore this, the effect of roughness height (RH) on airfoil performance is further analyzed, as illustrated in Figure 14. At low roughness heights (RH ≤ 0.05 mm), the lift coefficient curve closely mirrors that of a smooth airfoil, with both the lift slope and post-stall lift gradually decreasing as RH increases. This suggests that at low RH, the aerodynamic characteristics are only marginally affected, exhibiting a performance similar to that of a smooth airfoil, albeit with a slight decline. Conversely, at high roughness heights (RH ≥ 0.30 mm), the lift coefficient curve adopts a distinctive "N" shape, showing minimal variation with further increases in RH. This indicates that at high RH, aerodynamic performance is predominantly governed by the roughness, leading to a significantly altered and less efficient lift behavior that stabilizes in this new regime. For medium roughness heights (0.07 mm ≤ RH ≤ 0.10 mm), an intermediate condition emerges, characterized by unstable flow behavior as the angle of attack (AOA) increases, resulting in multiple saltation points in the lift curve. This reflects a transitional state where aerodynamic performance is neither fully smooth nor fully rough, leading to fluctuating and unstable lift characteristics.
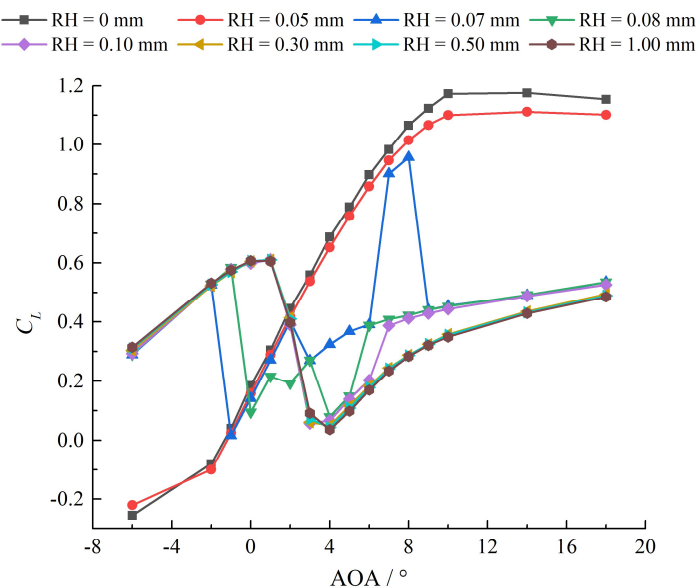
Figure 14. Lift coefficient of the rough airfoil with different roughness heights.

According to the continuity and smoothness of the lift coefficient curves in Figure 14, four distinct flow regimes can be identified, as illustrated in Figure 15. The classification of these flow regimes under varying roughness heights is summarized in Figure 16. The primary characteristics of these flow regimes are detailed as follows:

The Type 1 Flow Regime primarily occurs on relatively smooth airfoils (RH ≤ 0.05 mm). The flow patterns with increasing AOA are similar to those observed on traditional thin airfoils, as depicted in Figure 10. As the AOA increases from −6° to 18°, the flow undergoes a transition from trailing-edge separation on the lower surface to full attachment and finally to trailing-edge separation on the upper surface. The value of the lift coefficient decreases with increasing roughness, which is also similar to the behavior observed on traditional thin airfoils.

The Type 2 Flow Regime is mainly observed at small negative angles on rough airfoils (RH ≥ 0.30 mm). The trailing-edge separation vortex on the lower surface is relatively stable. As the AOA increases, the adverse pressure gradient on the upper surface increases, leading to a corresponding rise in the lift coefficient, as depicted in Figure 11a,b. The lift coefficient in this regime is relatively insensitive to variations in roughness height.

The Type 3 Flow Regime is mainly observed at positive angles on rough airfoils (RH ≥ 0.30 mm). The trailing-edge separation vortex on the upper surface enlarges with increasing AOA (Figure 11c,d), which plays a dominant role in lift performance. The scale of the separation vortex is larger than that at a same AOA in the Type 1 Flow Regime, leading to a relatively low lift coefficient. The Type 3 Flow Regime typically follows the Type 2 Flow Regime, with an abrupt transition between the two, giving rise to the characteristic "N" shape in the lift coefficient curve.

The Type 4 Flow Regime is primarily observed on airfoils with medium roughness heights (0.07 mm ≤ RH ≤ 0.10 mm). The overall trend of the lift curve is similar to Type 3 but slightly higher. This difference is attributed to the flow on the lower surface not being fully turbulent, as confirmed by wall shear analysis in Figure 17. It is shown that the flow is fully turbulent for RH = 0.3 mm, while an evident transition can be observed around half the chord on the lower surface for RH = 0.1 mm.

These four flow regimes illustrate how varying roughness heights influence the aerodynamic performance of airfoils, resulting in distinct lift characteristics under different conditions.
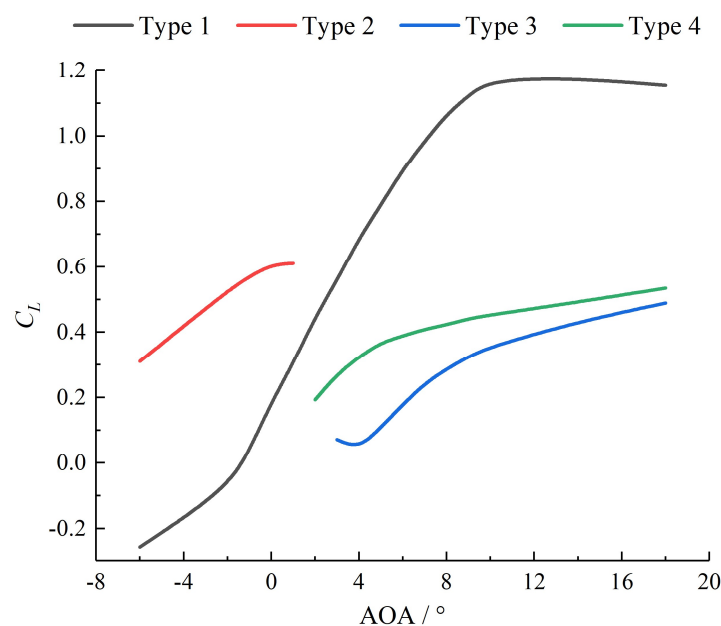
Figure 15. Definition of different flow regimes based on different lift curve segments.
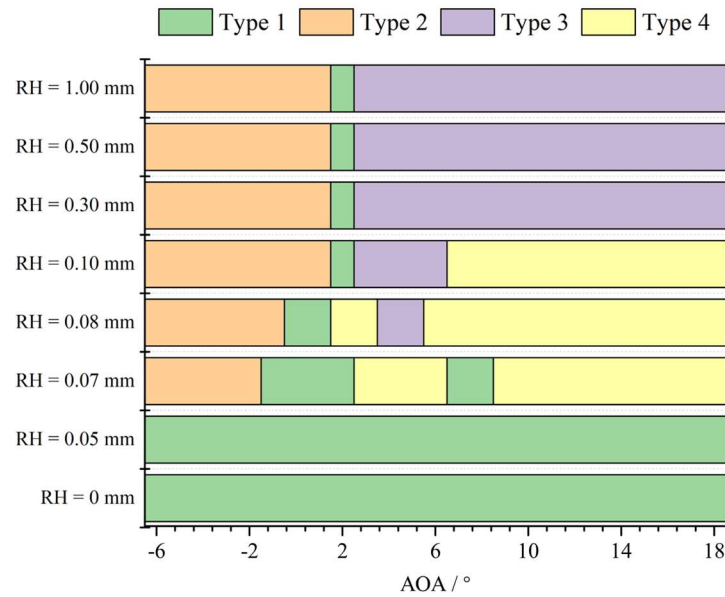
Figure 16. Influence of roughness height on different flow regimes.
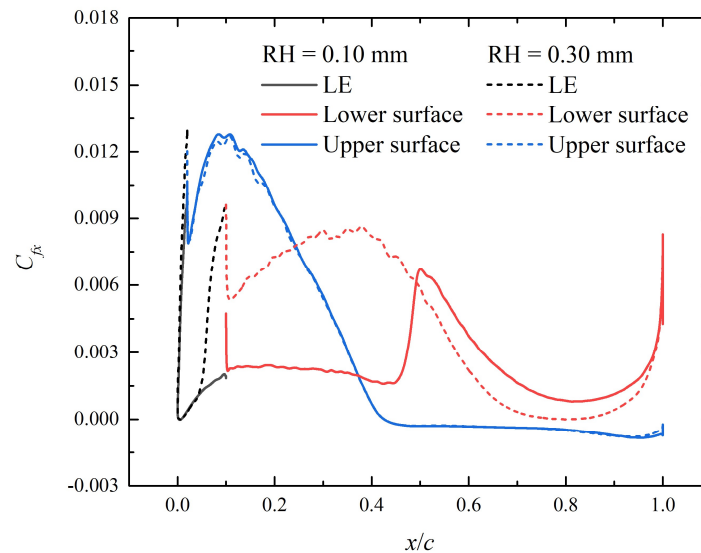
Figure 17. Nondimensional streamwise wall shear around the rough airfoil at 10° AOA (RH = 0.10 mm and 0.30 mm).

4. Conclusions

This study conducts numerical simulations on the DU 00-W-401 airfoil to explore the effects of leading-edge roughness. A simulation method that incorporates leading-edge roughness has been applied and verified as effective in capturing the primary characteristics induced by such roughness. The results reveal that the rough airfoil exhibits a distinctive "N"-shaped lift coefficient curve. This nonlinear lift curve is primarily due to the development of the trailing-edge separation vortex and variations in the adverse pressure gradient from the maximum thickness position to the trailing-edge confluence.

The impact of different roughness heights is also investigated. It is found that with a roughness height below 0.07 mm, the lift curve of the rough airfoil trends similarly to that of a smooth airfoil, though with a decreased lift coefficient. For roughness heights exceeding 0.3 mm, the boundary layer is fully turbulent, and the "N"-shaped lift curve becomes stable. Roughness heights between 0.07 mm and 0.1 mm result in a transitional state with several saltation points on the lift curve. This study summarizes the main characteristics of different flow regimes based on these varying lift curve segments.

The practical applications of this research are twofold. First, it introduces a simulation method that accounts for leading-edge roughness, which can be utilized to evaluate the aerodynamic performance of large-scale wind turbine blades under rough edge conditions. Second, it provides guidelines for selecting appropriate leading-edge roughness parameters in wind tunnel experiments. Future research will focus on how leading-edge roughness influences the development of three-dimensional separation vortices and impacts the aerodynamic performance of large-scale wind turbine blades. Overall, this study enhances the understanding of leading-edge roughness effects on the aerodynamic performance of thick airfoils, thereby contributing to advancements in wind turbine technology and promoting the broader adoption of renewable energy.

Author Contributions: Conceptualization, W.Z. and Q.L.; methodology, K.M., C.C. and J.Z.; software, K.M. and J.Z.; validation, X.S.; investigation, W.Z., X.S. and X.Z.; resources, J.Z. and X.R.; writing—original draft preparation, W.Z. and C.C.; writing—review and editing, X.S., W.Z. and Q.L.; visualization, K.M.; supervision, Q.L.; project administration, X.R.; funding acquisition, C.C. and Q.L. All authors have read and agreed to the published version of the manuscript.

Institutional Review Board Statement: Not applicable.

Informed Consent Statement: Not applicable.

Data Availability Statement: The raw data supporting the conclusions of this article will be made available by the authors on request.

Conflicts of Interest: Author Wei Zhang was employed by the company Hangzhou Huadian Engineering Consulting Co., Ltd. Authors Kuichao Ma and Jun Zhang were employed by the company Huadian Electric Power Research Institute Co., Ltd. The remaining authors declare that the research was conducted in the absence of any commercial or financial relationships that could be construed as a potential conflict of interest.

References

1. Hansen, M.O.L. *Aerodynamics of Wind Turbines*; Routledge: Oxfordshire, UK, 2008.
2. Madsen, H.A.; Bak, C.; Døssing, M.; Johansen, J. Influence of Airfoil Aerodynamics on Wind Turbine Performance. *Wind Energy* **2010**, *13*, 373–386. [CrossRef]
3. Selig, M.S.; McGranahan, B.D. Wind Tunnel Aerodynamic Tests of Six Airfoils for Use on Small Wind Turbines. *J. Sol. Energy Eng.* **2004**, *126*, 986–1001. [CrossRef]
4. Buhl, M.L.; Manwell, J.F. A Review of Aerodynamic Models for Wind Turbines. *Renew. Energy* **2005**, *30*, 1779–1798.
5. Tangler, J.L.; Somers, D.M. *NREL Airfoil Families for HAWTs*; No. NREL/TP-442-7109; National Renewable Energy Laboratory (NREL): Golden, CO, USA, 1995.
6. Timmer, W.A.; van Rooij, R. Summary of the Delft University wind turbine dedicated airfoils. *J. Sol. Energy Eng.* **2003**, *125*, 488–496. [CrossRef]
7. Bjork, A. *Coordinates and Calculations for the FFA-W1-xxx, FFA-W2-xxx and FFA-W3-xxx Series of Airfoils for Horizontal Axis Wind Turbines*; FFA TN 1990-15; Aeronautical Research Institute of Sweden: Stockholm, Sweden, 1990.
8. Fuglsang, P.; Bak, C. Development of the Risøwind turbine airfoils. *Wind Energy* **2004**, *7*, 145–162. [CrossRef]
9. Fuglsang, P.; Madsen, H.A. Optimization of Wind Turbine Rotors Using Risø-A1 Airfoils. *J. Sol. Energy Eng.* **1999**, *121*, 129–135.
10. Berg, D.E. *Airfoil Design Catalog*; Sandia National Laboratories: Albuquerque, NM, USA, 2001; Volume 1.
11. Bak, C.; Johansen, J.; Fuglsang, P. *Wind Tunnel Tests of the Risø-A1-18, Risø-A1-21 and Risø-A1-24 Airfoils*; Risø National Laboratory: Roskilde, Denmark, 2000.
12. Bach, J.; Vitale, G. The Influence of Leading-Edge Roughness on Wind Turbine Airfoil Performance. *Renew. Energy* **2022**, *176*, 1123–1135.
13. Mueller, T.J. Aerodynamic Measurements at Low Reynolds Numbers for Fixed Wing Micro-Air Vehicles. *Exp. Fluids* **2003**, *34*, 687–693.
14. Sareen, A.; Sapre, C.A.; Selig, M.S. Effects of Leading Edge Roughness on Airfoil Performance. *Wind Eng.* **2014**, *38*, 529–547.

15. Brooks, T.F.; Marcolini, M.A.; Pope, D.S. Airfoil Self-Noise and Prediction. In *NASA Reference Publication 1218*; NASA: Washington, DC, USA, 1989.
16. Bons, J.P. A Review of Surface Roughness Effects in Gas Turbines. *J. Turbomach.* **2010**, *132*, 041012. [CrossRef]
17. Van Rooij, R.; Timmer, W.A. Roughness sensitivity considerations for thick rotor blade airfoils. *J. Sol. Energy Eng.* **2003**, *125*, 468–478. [CrossRef]
18. Baker, J.P.; Mayda, E.A.; van Dam, C.P. Experimental Analysis of Thick Blunt Trailing-Edge Wind Turbine Airfoils. *J. Sol. Energy Eng.* **2006**, *128*, 422–431. [CrossRef]
19. Hansen, K.L.; Kelso, R.M.; Dally, B.B. Performance Variations of Leading-Edge Tubercles for Distinct Airfoil Profiles. *AIAA J.* **2011**, *49*, 185–194. [CrossRef]
20. Cai, C.; Zuo, Z.; Maeda, T.; Kamada, Y.; Li, Q.; Shimamoto, K.; Liu, S. Periodic and aperiodic flow patterns around an airfoil with leading-edge protuberances. *Phys. Fluids* **2017**, *29*, 115110. [CrossRef]
21. Hansen, K.L.; Rostamzadeh, N.; Kelso, R.M.; Dally, B.B. Evolution of the streamwise vortices generated between leading edge tubercles. *J. Fluid Mech.* **2016**, *788*, 730–766. [CrossRef]
22. Menter, F.R.; Langtry, R.B.; Likki, S.R.; Suzen, Y.B.; Huang, P.G.; Völker, S. A correlation-based transition model using local variables—Part I: Model formulation. *J. Turbomach.* **2006**, *128*, 413–422. [CrossRef]
23. Langtry, R.B.; Menter, F.R. Correlation-based transition modeling for unstructured parallelized computational fluid dynamics codes. *AIAA J.* **2009**, *47*, 2894–2906. [CrossRef]
24. White, F.M.; Majdalani, J. *Viscous Fluid Flow*; McGraw-Hill: New York, NY, USA, 2006.
25. Fluent, A. *Ansys Fluent Theory Guide*; Ansys Inc.: Canonsburg, PA, USA, 2011; Volume 15317, pp. 724–746.